

## SUPPORTING INFORMATION

### High Thermoelectric Performance in Crystallographically Textured $n$ -type $\text{Bi}_2\text{Te}_{3-x}\text{Se}_x$ Produced from Asymmetric Colloidal Nanocrystals

*Yu Liu,<sup>†</sup> Yu Zhang,<sup>†</sup> Khak Ho Lim,<sup>‡</sup> Maria Ibáñez,<sup>§, ⊥</sup> Silvia Ortega,<sup>†</sup> Mengyao Li,<sup>†</sup> Jérémy David,<sup>¶</sup>  
Sara Martí-Sánchez,<sup>¶</sup> Ka Ming Ng,<sup>‡</sup> Jordi Arbiol,<sup>¶, //</sup> Maksym V. Kovalenko,<sup>§, ⊥</sup> Doris Cadavid,<sup>\*, †</sup>  
<sup>○</sup> Andreu Cabot<sup>\*, †, //</sup>*

<sup>†</sup> Catalonia Energy Research Institute - IREC, Sant Adria de Besòs, 08930 Barcelona, Spain.

<sup>‡</sup> Department of Chemical and Biological Engineering, Hong Kong University of Science and Technology, Hong Kong, China.

<sup>§</sup> Institute of Inorganic Chemistry, Department of Chemistry and Applied Biosciences, ETH Zürich, Vladimir Prelog Weg 1, CH-8093, Switzerland.

<sup>⊥</sup> Empa – Swiss Federal Laboratories for Materials Science and Technology, Dübendorf, Überlandstrasse 129, CH-8600, Switzerland.

<sup>¶</sup> Catalan Institute of Nanoscience and Nanotechnology (ICN2), CSIC and BIST, Campus UAB, Bellaterra, 08193 Barcelona, Catalonia, Spain.

<sup>//</sup> ICREA, Pg. Lluís Companys 23, 08010 Barcelona, Spain.

<sup>○</sup> Departamento de Física, Universidad Nacional de Colombia, 111321, Ciudad Universitaria, Bogotá, Colombia.

\* Email: [acabot@irec.cat](mailto:acabot@irec.cat)

\* Email: [dycadavidr@unal.edu.co](mailto:dycadavidr@unal.edu.co)

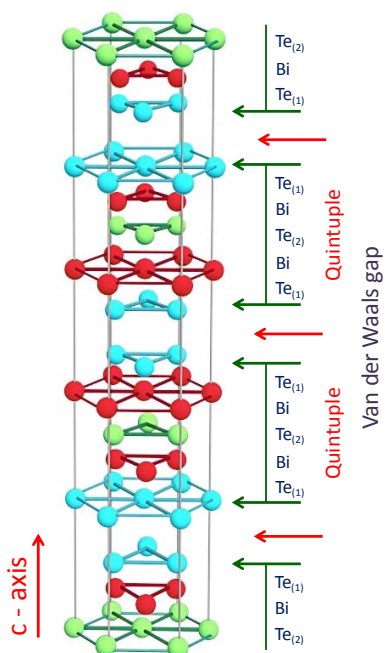


**Figure S1.** Crystal structure of bismuth telluride ( $\text{Bi}_2\text{Te}_3$ ).

**Table S1.** Crystallographic parameters of  $\text{Bi}_2\text{Te}_3$ .<sup>1</sup>

Crystallographic parameters	Values
Reference code	01-089-2009
Crystal system	Rhombohedral
Space group	$R\bar{3}m$
Space group number	166
a (Å)	4.3860
b (Å)	4.3860
c (Å)	30.4970
Alpha (°)	90
Beta (°)	90
Gamma (°)	120
Volume of cell ( $10^{-6} \text{ pm}^3$ )	508.07
Theoretical calculated density ( $\text{g/cm}^3$ )	7.85

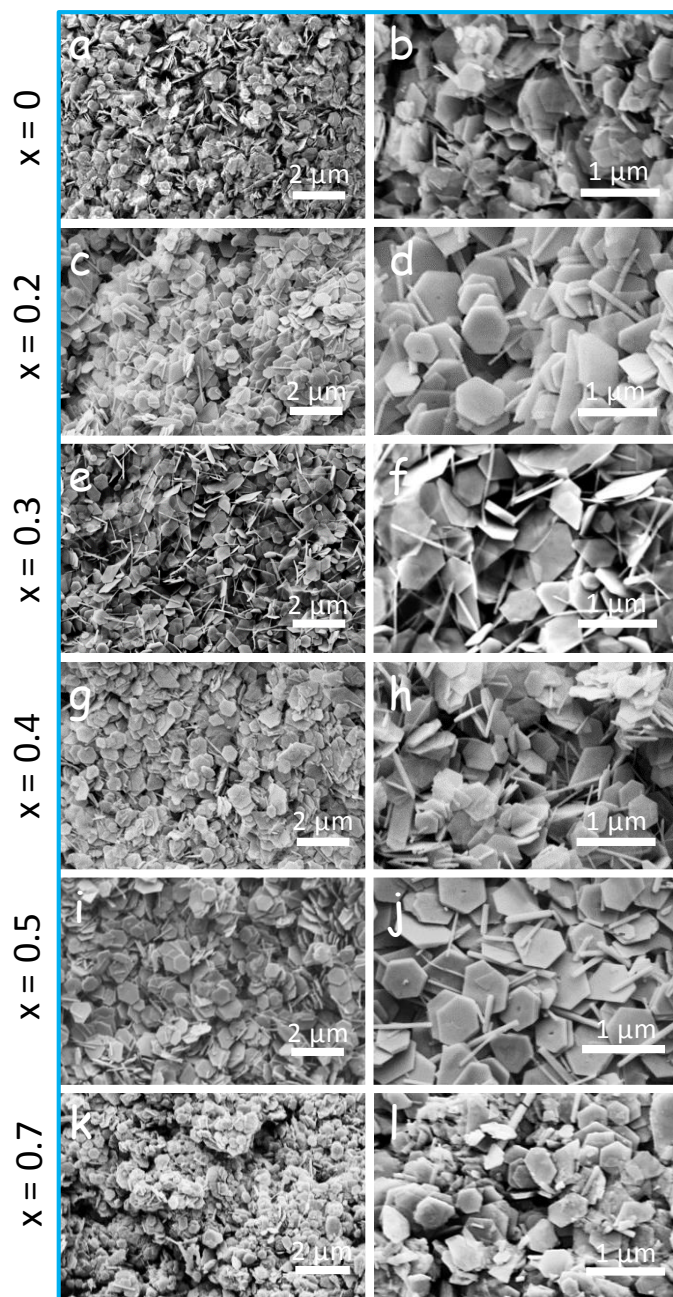


**Figure S2.** Representative SEM micrographs of  $\text{Bi}_2\text{Te}_{3-x}\text{Se}_x$  NCs synthesized at the 25 mol% excess of Te: (a), (b)  $x = 0$ ; (c), (d)  $x = 0.2$ ; (e), (f)  $x = 0.3$ ; (g), (h)  $x = 0.4$ ; (i), (j)  $x = 0.5$  and (k), (l)  $x = 0.7$ .

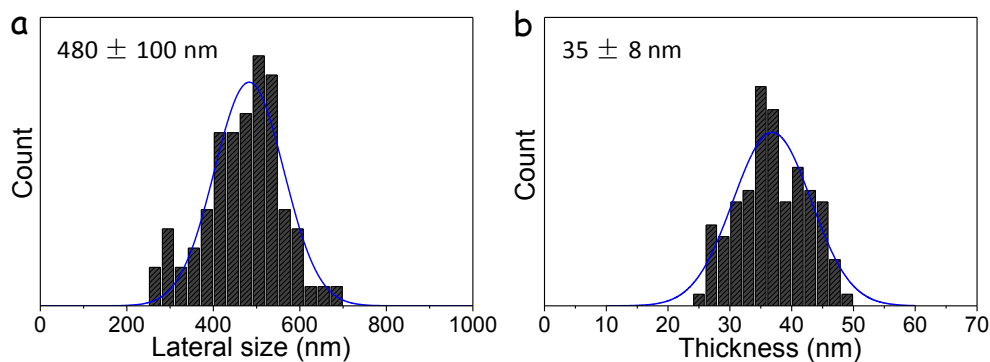


**Figure S3** a) and b) Statistical lateral size and thickness distributions of  $\text{Bi}_2\text{Te}_{2.7}\text{Se}_{0.3}$  nanodisks, respectively. The lateral average size of the nanodisks did not significantly change with the Se concentration

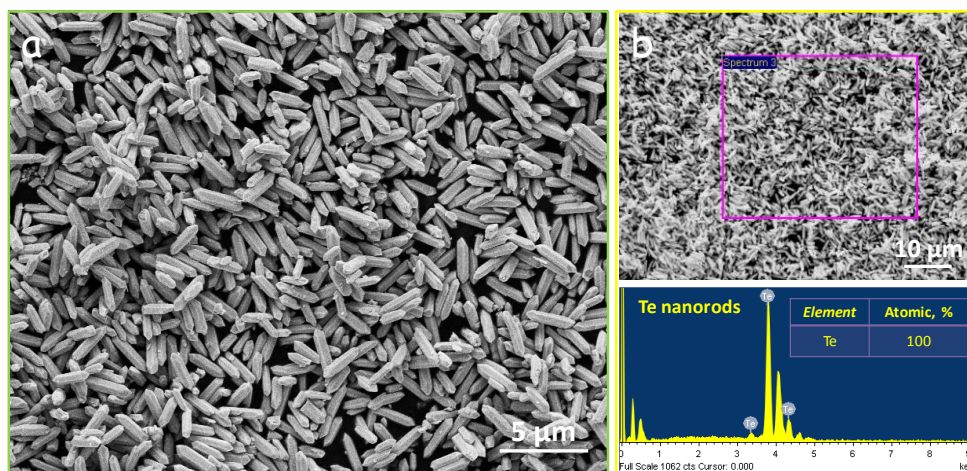


**Figure S4.** Representative SEM micrograph and EDX patent of the Te nanorods produced from the reduction of the Te precursor ( $\text{Na}_2\text{TeO}_3$ ) in the exact same conditions as those used to produce  $\text{Bi}_2\text{Te}_{3-x}\text{Se}_x$  NCs, but in the absence of the Bi and Se precursors.

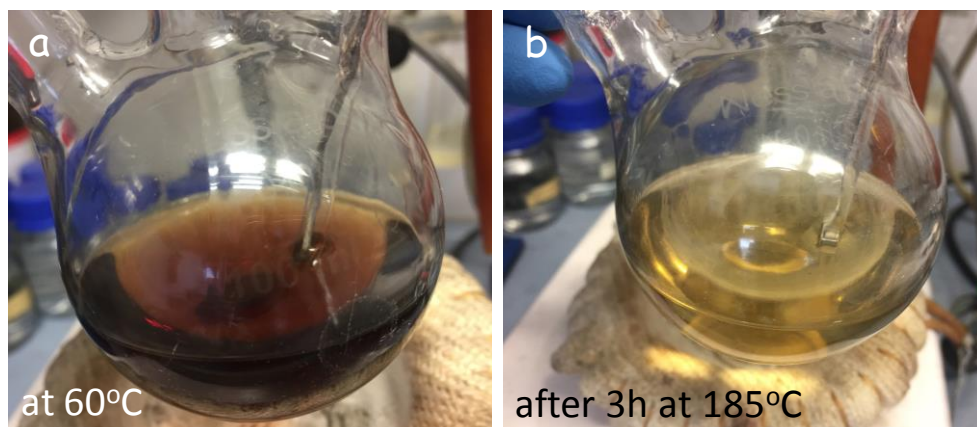


**Figure S5.** Optical photographs of the solution of Se before and after reaction. In the exact same conditions, *e.g.* reaction time, temperature, chemicals and solvent as those used to produce  $\text{Bi}_2\text{Te}_{3-x}\text{Se}_x$  NCs, the reaction of the Se precursor  $\text{Na}_2\text{SeO}_3$  alone (without Bi and Se precursors) didn't result in the formation of Se particles. A clear solution was obtained after 3 h at 185 °C.

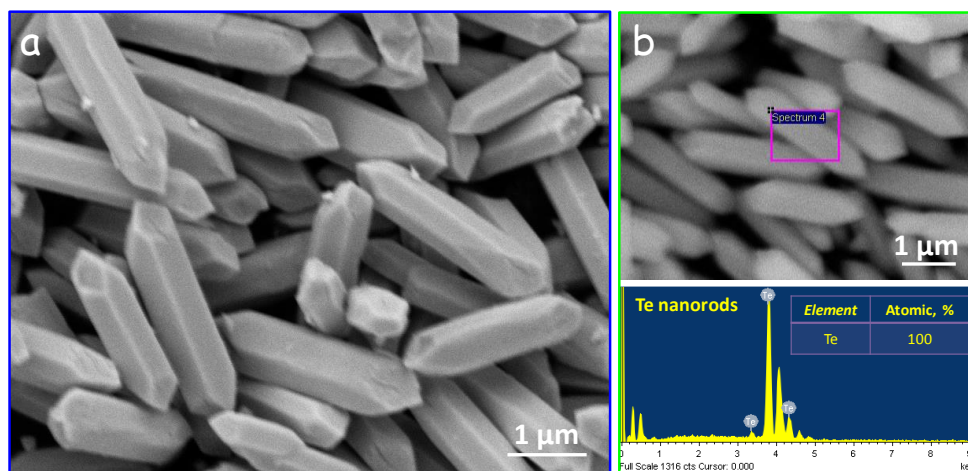


**Figure S6.** Representative SEM micrograph and EDX patent of the Te nanorods produced from the reduction of the Te precursor ( $\text{Na}_2\text{TeO}_3$ ) and the Se precursor ( $\text{Na}_2\text{SeO}_3$ ) in the exact same conditions as those used to produce  $\text{Bi}_2\text{Te}_{3-x}\text{Se}_x$  NCs, but in the absence of the Bi precursor. Pure Te nanorods were obtained.



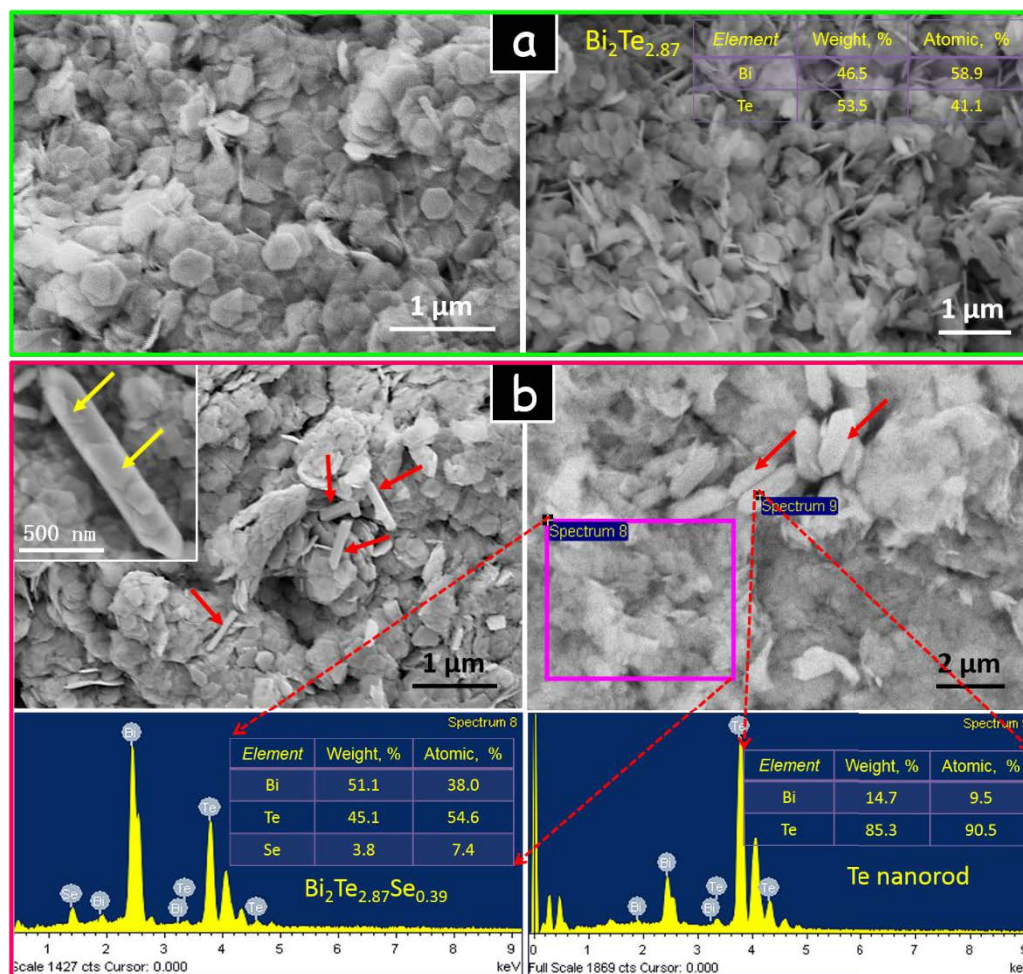


**Figure S7.** (a) SEM micrographs and EDX analysis results of  $\text{Bi}_2\text{Te}_3$  nanodisks obtain in the same conditions as  $\text{Bi}_2\text{Te}_{3-x}\text{Se}_x$  nanodisks but in the absence of Se precursor. (b) SEM micrograph and EDX spectra of the  $\text{Bi}_2\text{Te}_{3-x}\text{Se}_x$  nanodisks obtained from the reaction of  $\text{Bi}_2\text{Te}_3$  nanodisks with the Se precursor ( $\text{Na}_2\text{SeO}_3$ ) at 185  $^\circ\text{C}$  for 3h. Te nanorods are observed to appear after reaction.

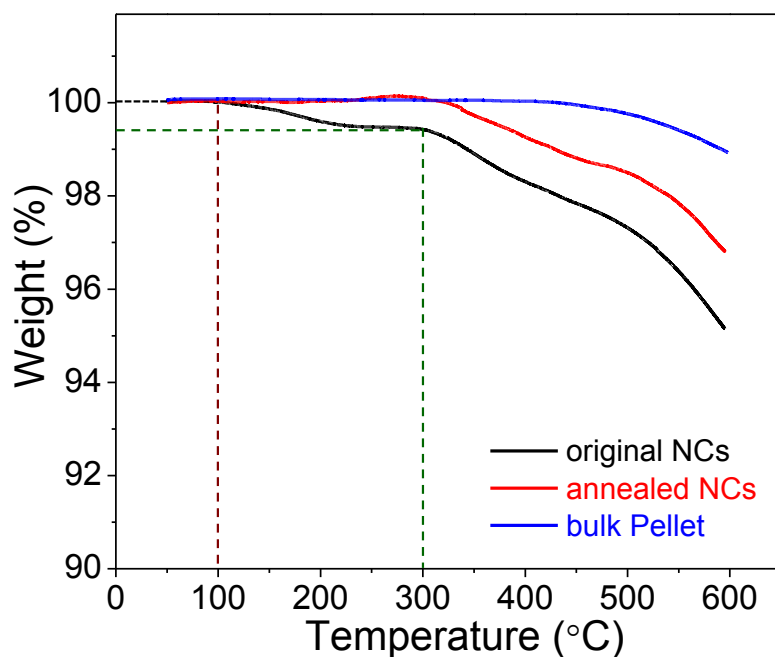


**Figure S8.** Thermogravimetric analysis (TGA) profile obtained from the original NCs, annealed NCs and bulk pellets using a heating rate of 10°C/min under N<sub>2</sub> flow. The evaporation/removal of PVP took place in the temperature range from 100 °C to 300 °C. Only the original NCs showed this weight loss. Above 300 °C a second step was observed for both NC samples containing excess amounts of Te. We associated this decrease to the Te removal. At temperatures above 450 °C another weight loss step was observed for all samples. We associate this one to the removal of lattice chalcogens.

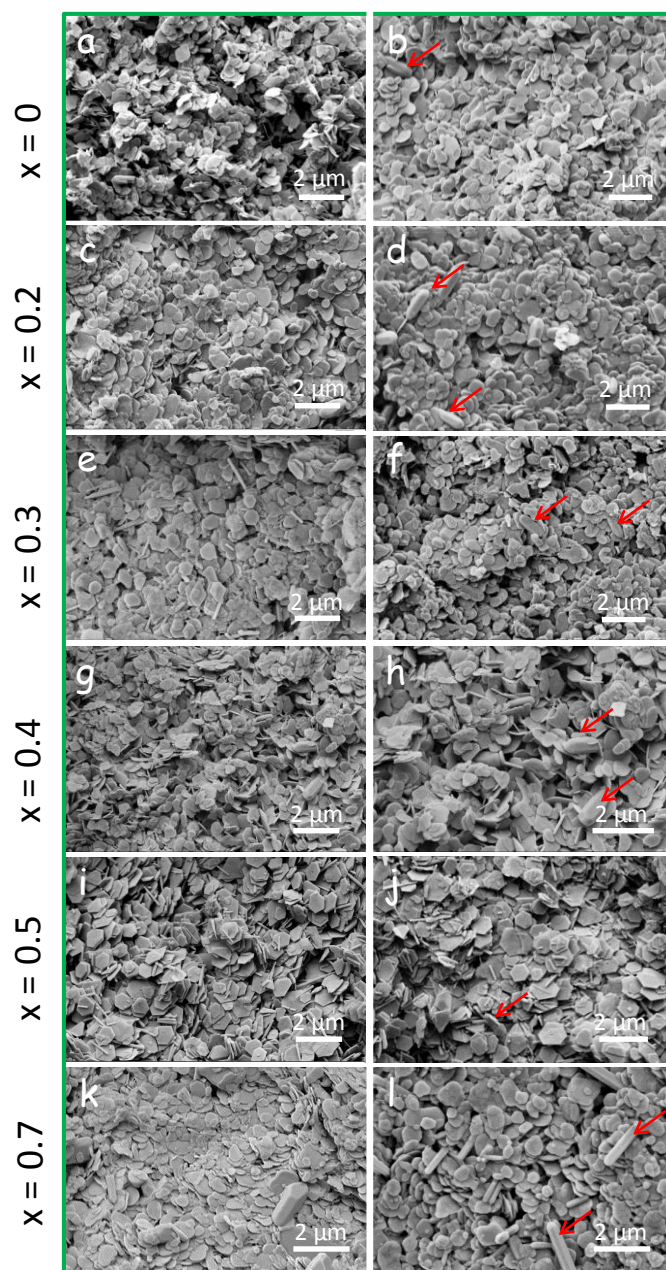


**Figure S9.** Representative SEM micrographs of  $\text{Bi}_2\text{Te}_{3-x}\text{Se}_x$  NCs with 25 mol% excess of tellurium after annealing at 350 °C for 1 h: (a), (b)  $x = 0$ ; (c), (d)  $x = 0.2$ ; (e), (f)  $x = 0.3$ ; (g), (h)  $x = 0.4$ ; (i), (j)  $x = 0.5$  and (k), (l)  $x = 0.7$ .



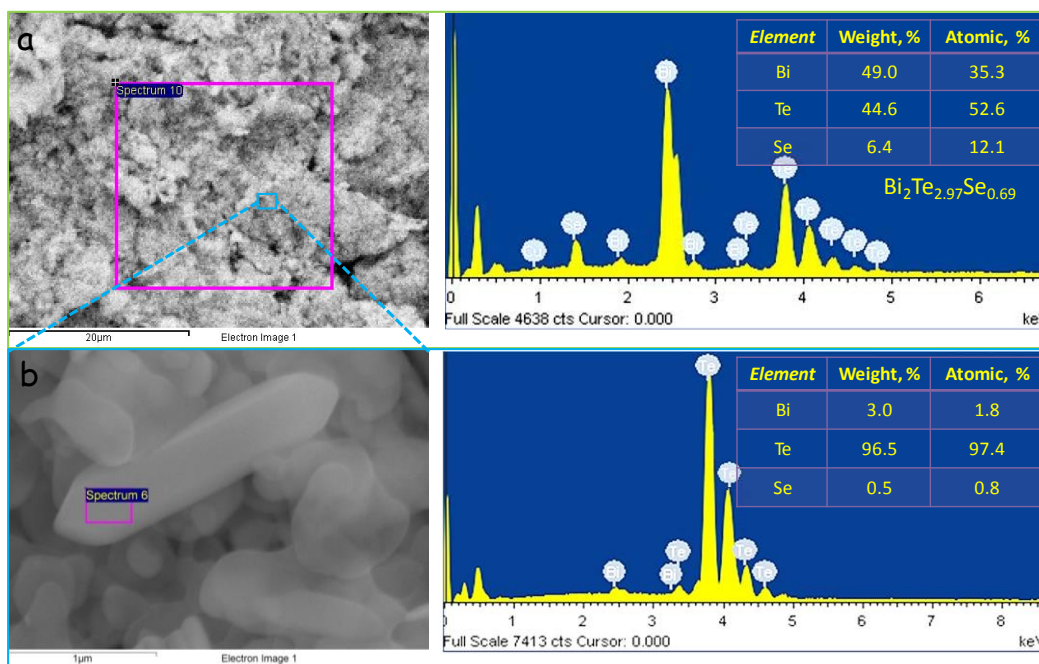


**Figure S10.** a) SEM and SEM-EDX spectrum of annealed  $\text{Bi}_2\text{Te}_{2.3}\text{Se}_{0.7}$ ; b) SEM and SEM-EDX spectrum of a large Te nanorod observed in the same sample.

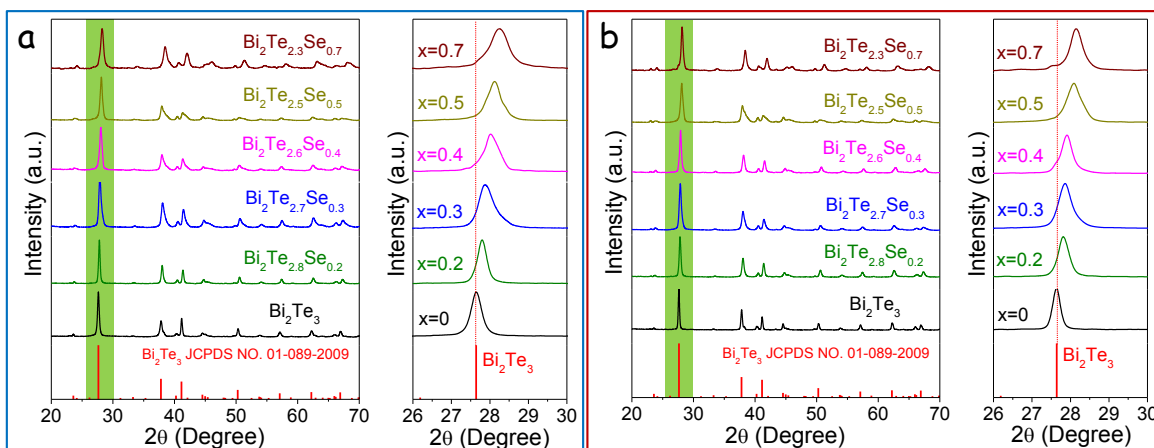


**Figure S11.** XRD patterns of  $\text{Bi}_2\text{Te}_{3-x}\text{Se}_x$  (x = 0, 0.2, 0.3, 0.4, 0.5 and 0.7) NCs before (a) and after (b) annealing at 350 °C for 60 min. Detail of the same XRD patterns showing the systematic shift of the (015) peak with the Se composition (x) is also provided. The standard  $\text{Bi}_2\text{Te}_3$  diffraction pattern (JCPDS NO. 01-089-2009) is also included as reference.

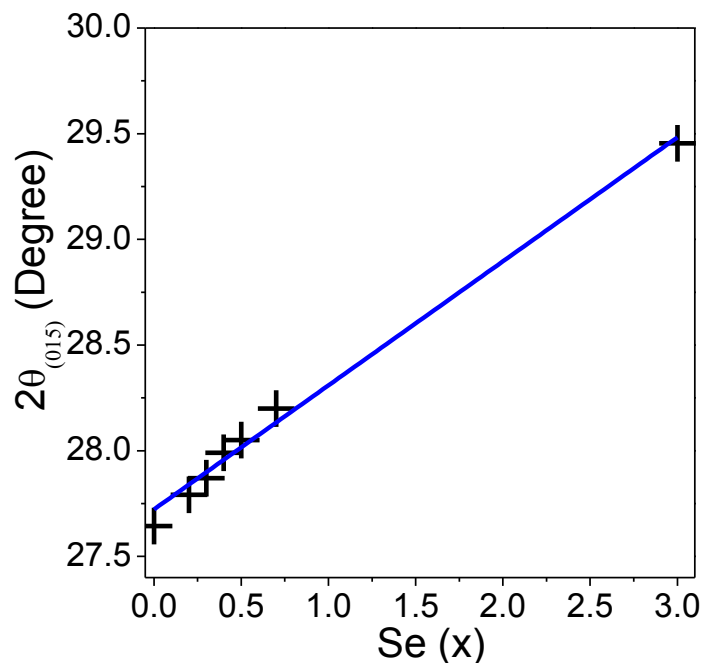


**Figure S12.** Dependence of (015) XRD peak with the Se concentration (x) of  $\text{Bi}_2\text{Te}_{3-x}\text{Se}_x$  NCs showing them to follow the Vegard's law.

**Table S2,** Relative densities of  $\text{Bi}_2\text{Te}_{3-x}\text{Se}_x$  pellets obtained from absolute values measured with the Archimedes' method and the linear regression of the theoretical values between  $\text{Bi}_2\text{Te}_3$  and  $\text{Bi}_2\text{Se}_3$ .

Sample	x=0	x=0.2	x=0.3	x=0.4	x=0.5	x=0.7
Crystal density (linear regression, $\text{g/cm}^3$ )	7.85	7.83	7.82	7.80	7.79	7.77
Measured density ( $\text{g/cm}^3$ )	7.32	7.25	7.28	7.35	7.24	7.19
Relative density (%)	93.2%	92.6%	93.1%	94.2%	92.9%	92.5%

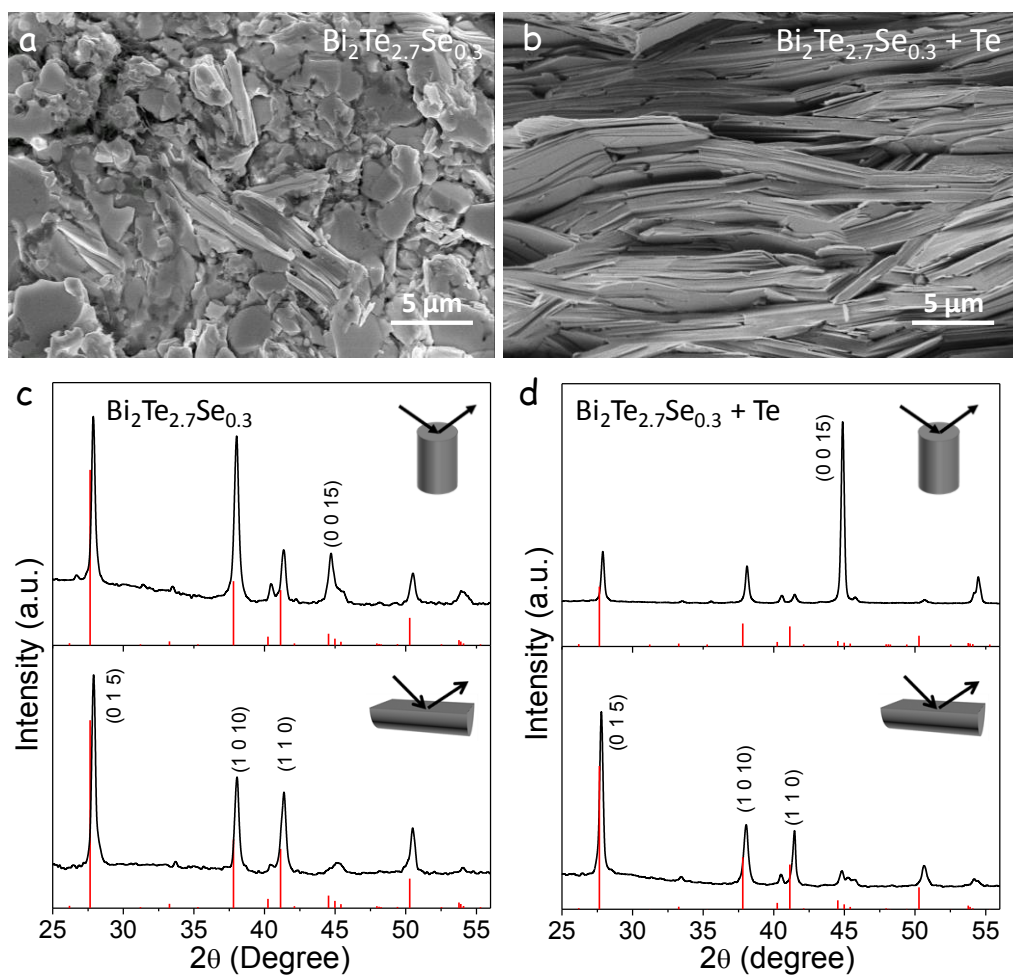


**Figure S13.** a), b) Cross-section SEM micrographs of the  $\text{Bi}_2\text{Te}_{2.7}\text{Se}_{0.3}$  pellets produced without (a) and with (b) an excess of tellurium in the initial NCs. c), d) XRD patterns of the  $\text{Bi}_2\text{Te}_{2.7}\text{Se}_{0.3}$  pellets produced without (c) and with (d) an excess of Te. Red vertical lines correspond to the reference literature data for  $\text{Bi}_2\text{Te}_3$ , JCPDS NO. 01-089-2009.

**Table 3.** SEM-EDX composition (related to Bi = 2) of the  $\text{Bi}_2\text{Te}_{2.7}\text{Se}_{0.3}$  NCs before and after annealing and the consolidated pellets. Data was obtained from averaging 5 analyses, resulting in an estimated error of *ca.* 3 %. No additional Te excess was introduced in this sample.

Nominal x Material	x = 0.3	
	Te	Se
NCs	2.72	0.29
Annealed NCs	2.71	0.29
Pellet	2.69	0.31

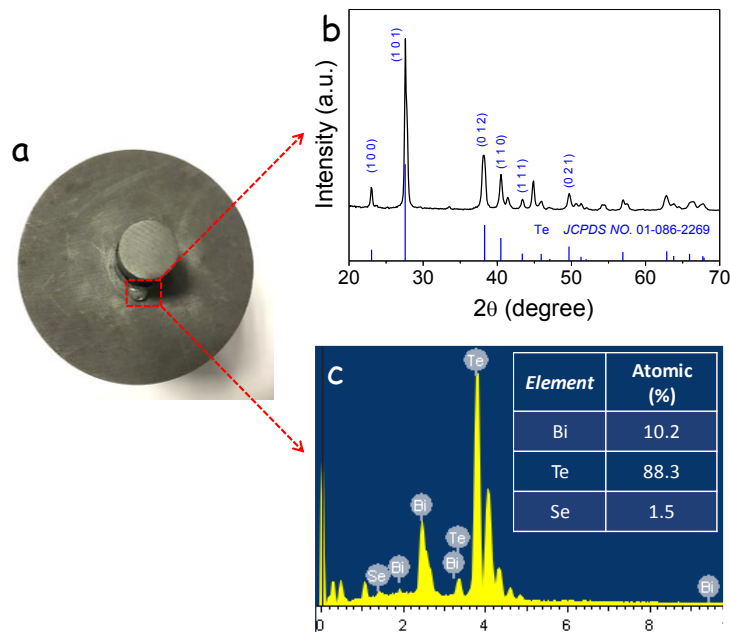


**Figure S14.** (a) Photograph of the graphite die and the carbon rod after hot press. As indicated by the red square, some material was expelled out from the die during the process. (b) XRD and (c) EDX data of the expelled material, confirming that it consisted mostly, ~90%, of tellurium.



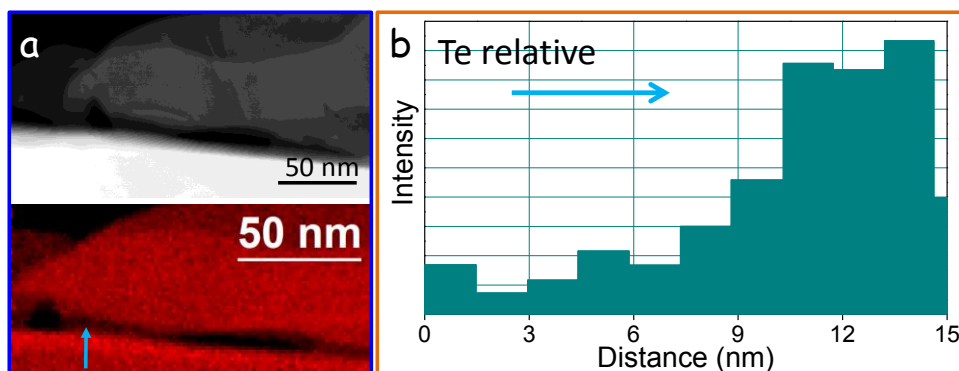


**Figure S15.** a) ADF-STEM (a, top) and STEM-EELS Te composition map (a, bottom) of the interface between two crystals; b) the relative Te intensity profile calculated along the cyan arrow in the EELS map.

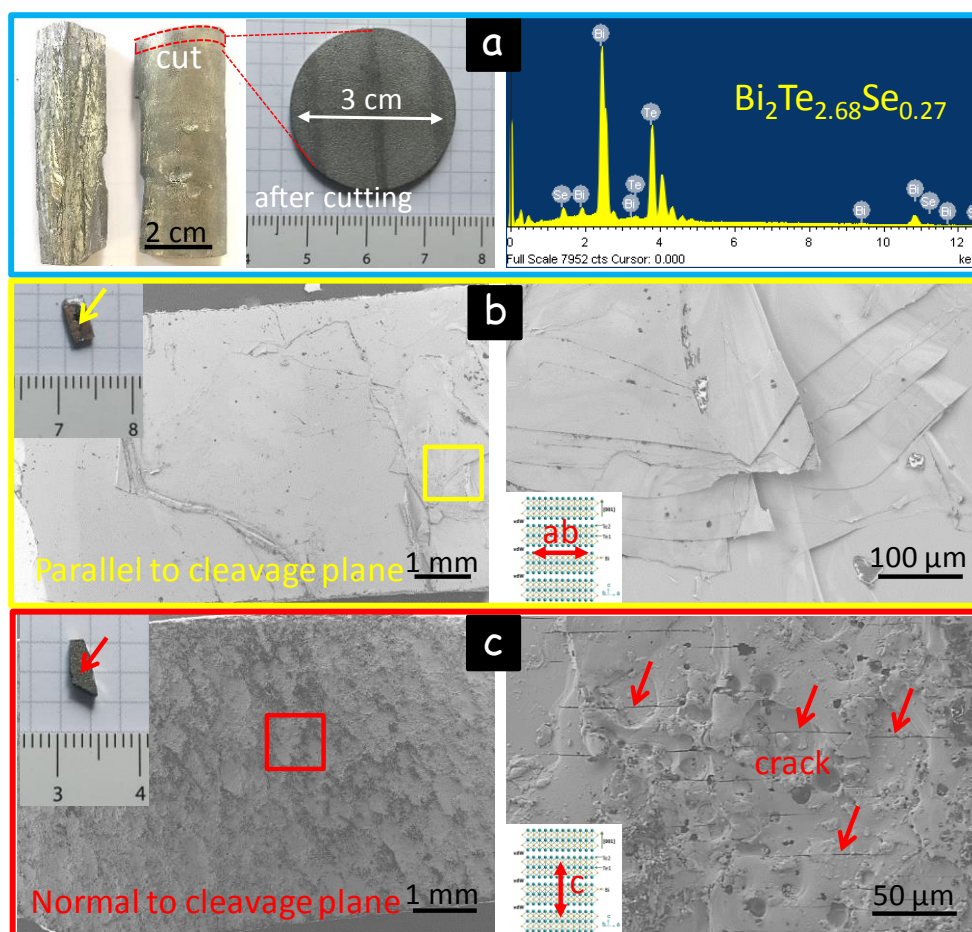


**Figure S16.** a) Optical image of the n-type commercial ingot, pieces of the ingots after the cutting process, and SEM-EDX composition. b) and c) SEM images of the commercial ingot from directions parallel and normal to the cleavage plane. Some cracks were found, as shown in Figure c.

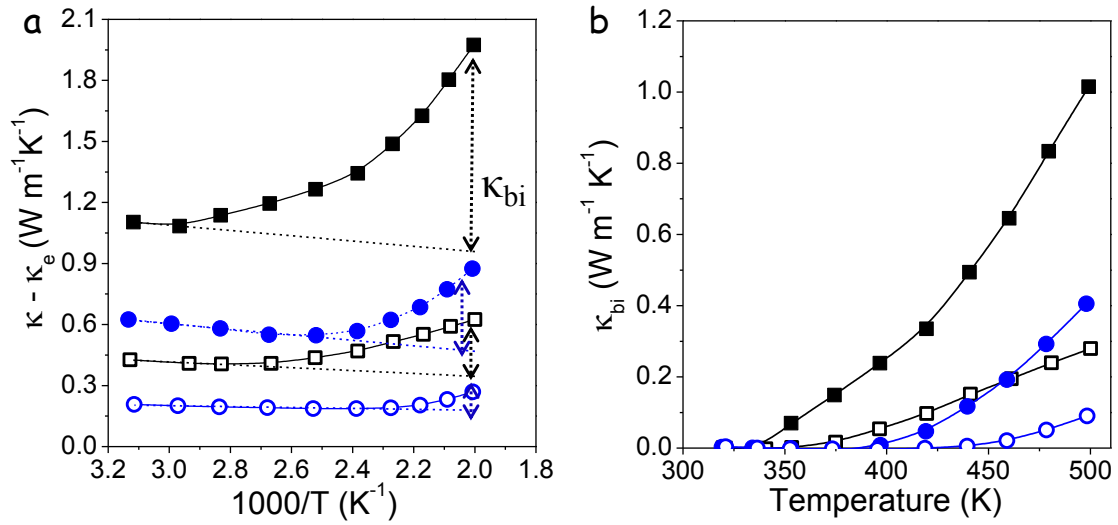


**Figure S17.** Temperature dependence of TE properties of  $\text{Bi}_2\text{Te}_{2.7}\text{Se}_{0.3}$  nanomaterials: (a)  $\kappa - \kappa_e$ ; and (b) bipolar component to the thermal conductivity,  $\kappa_{bi}$ , estimated as the difference between  $\kappa - \kappa_e$  and a linear fitting of  $\kappa - \kappa_e$  as a function of  $1/T$  in the low temperature range of the nanomaterial and the commercial ingot sample. The  $\text{Bi}_2\text{Te}_{2.7}\text{Se}_{0.3}$  nanomaterial hot pressed at 480 °C (blue circles) was measured in two directions, parallel (open circles,  $\circ$ ) and normal (solid circles,  $\bullet$ ) to the press axis. The plotted data were obtained by averaging the experimental data measured from five samples having approximately the same composition. The commercial ingot was measured in two directions, parallel (open black squares,  $\square$ ) and normal (solid black squares,  $\blacksquare$ ) to the  $c$  crystallographic direction.

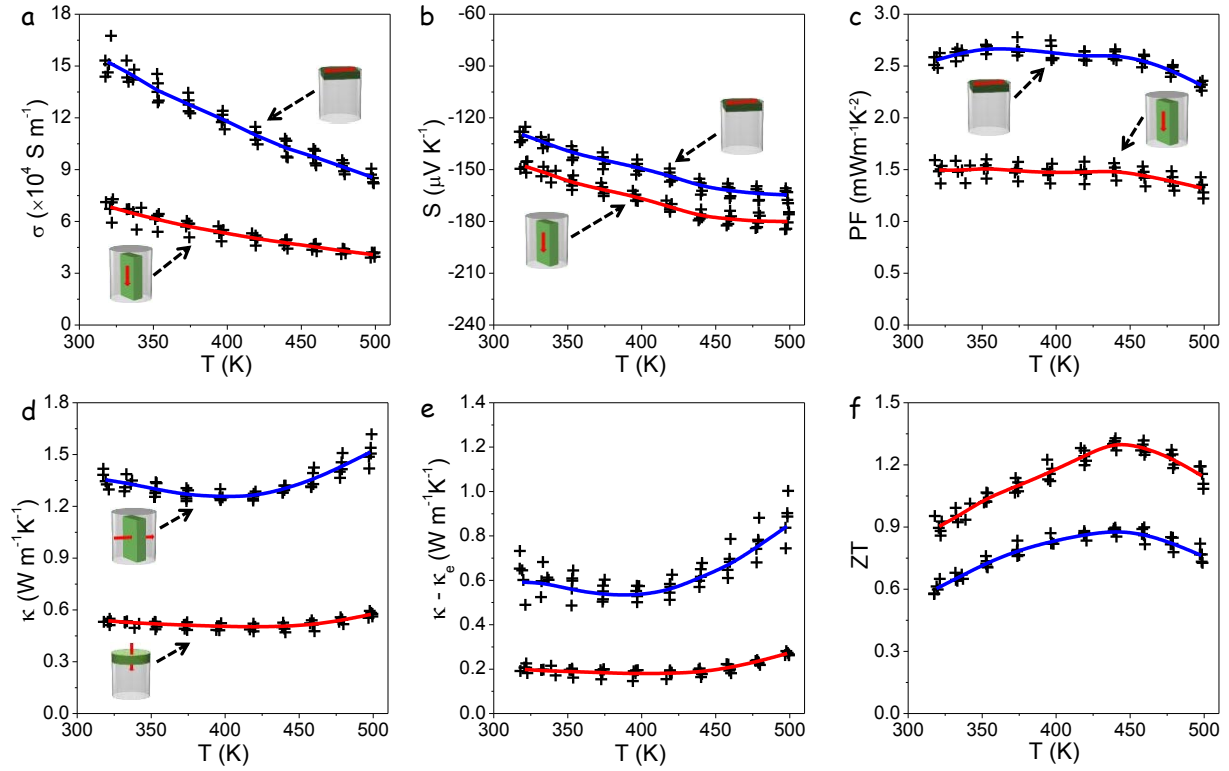


**Figure S18.** Temperature dependence of electrical conductivity,  $\sigma$  (a); Seebeck coefficient,  $S$  (b); thermal conductivity,  $\kappa$  (c); and TE figure of merit,  $ZT$  (d) of five  $\text{Bi}_2\text{Te}_{2.7}\text{Se}_{0.3}$  pellets measured in the direction parallel and normal to the pressing direction. Data from 5 samples is plotted with black crosses, and red and blue lines display the average values in the parallel and normal directions, respectively.

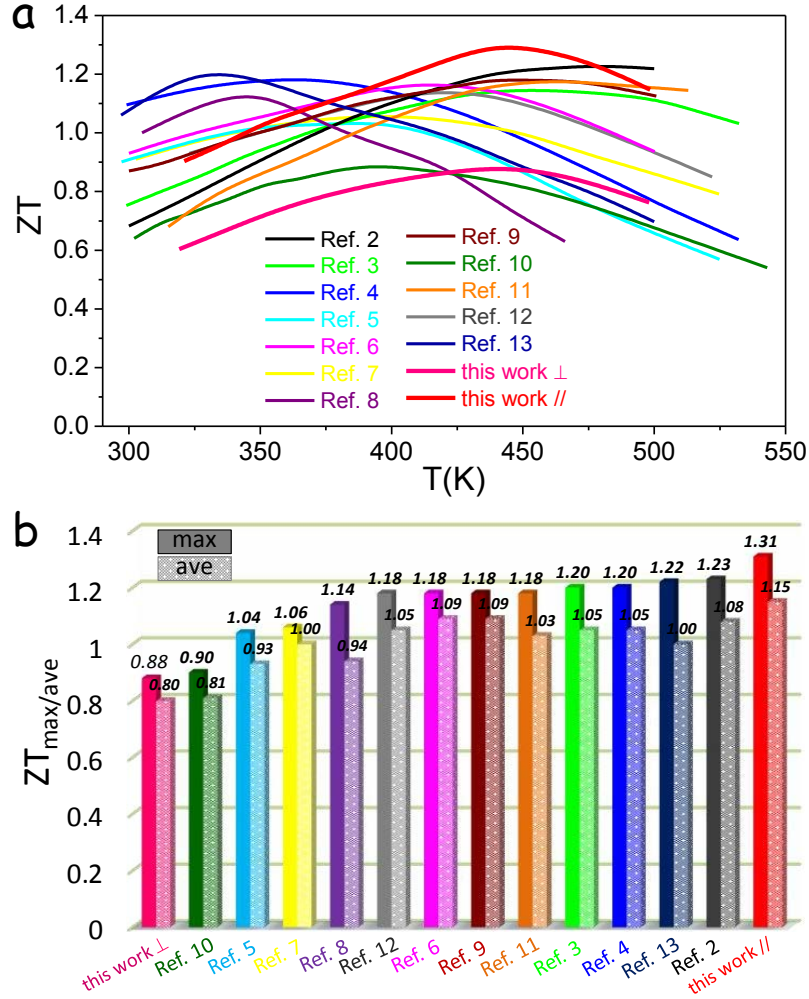


**Figure S19.** a) Temperature dependence of ZT values for state-of-the-art n-type Bi<sub>2</sub>Te<sub>3</sub>-based alloys. State-of-the-art maximum ZT values and average ZT values for n-type Bi<sub>2</sub>Te<sub>3</sub>-based alloys.<sup>2-13</sup> Our data is named as “this work ⊥” and “this work //”, corresponding to the values obtained from averaging the experimental data measured from 5 different samples in the two directions: perpendicular (⊥) and parallel (//) to the pressing direction, respectively. Average ZT values were calculated on the temperature range from 320 K to 500 K for all samples, except for reference 8 (320-465 K).



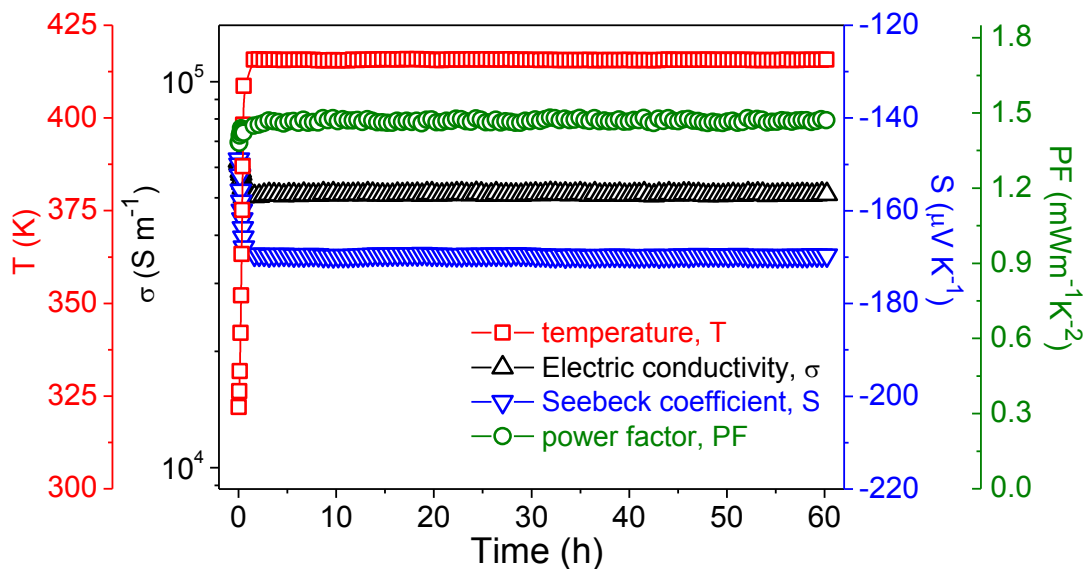


**Figure S20.** Evolution of the electrical conductivity ( $\sigma$ ), Seebeck coefficient ( $S$ ) and power factor ( $PF$ ) of the  $\text{Bi}_2\text{Te}_{2.7}\text{Se}_{0.3}$  sample measured in the // direction during a 60.2 h test at 420 K.

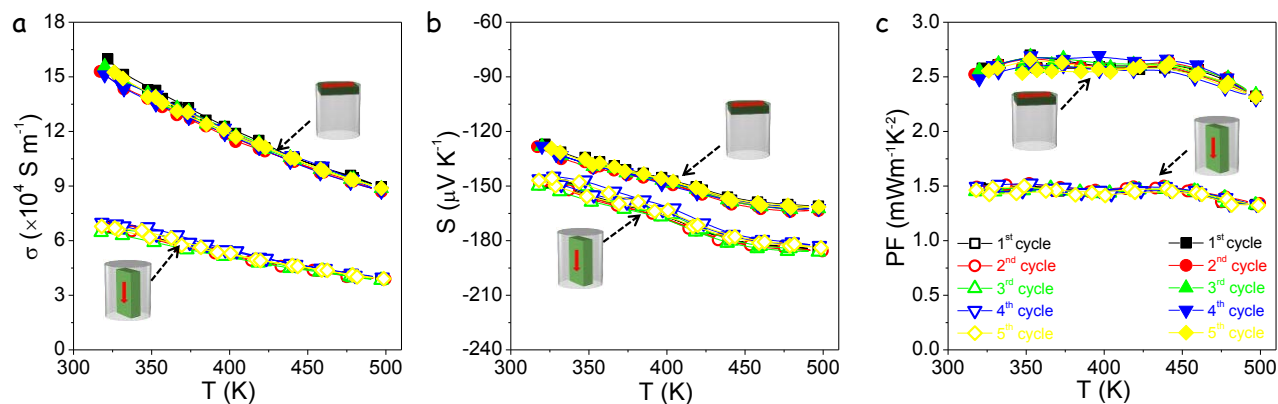


**Figure S21.** Temperature dependence of the electrical conductivity,  $\sigma$  (a), Seebeck coefficient,  $S$  (b), and power factor,  $PF$  (c) of a  $\text{Bi}_2\text{Te}_{2.7}\text{Se}_{0.3}$  pellet measured in the // direction for 5 consecutive up-down cycles heating-cooling cycles from room temperature to 498 K. No pre-stabilization treatment was carried out before the first measurement.

## References

1. Nakajima, S. The Crystal Structure of  $\text{Bi}_2\text{Te}_{3-x}\text{Se}_x$ . *J. Phys. Chem. Solids* **1963**, *24*, 479–485.
2. Hong, M.; Chasapis, T. C.; Chen, Z.-G.; Yang, L.; Kanatzidis, M. G.; Snyder, G. J.; Zou, J. *n*-Type  $\text{Bi}_2\text{Te}_{3-x}\text{Se}_x$  Nanoplates with Enhanced Thermoelectric Efficiency Driven by Wide-Frequency Phonon Scatterings and Synergistic Carrier Scatterings. *ACS nano* **2016**, *10*, 4719–4727.
3. Zhai, R.; Hu, L.; Wu, H.; Xu, Z.; Zhu, T.-J.; Zhao, X.-B. Enhancing Thermoelectric Performance of *n*-Type Hot Deformed Bismuth-Telluride-Based Solid Solutions by Nonstoichiometry-Mediated Intrinsic Point Defects. *ACS Appl. Mater. Interfaces* **2017**, *9*, 28577–28585.
4. Hu, L.; Wu, H.; Zhu, T.; Fu, C.; He, J.; Ying, P.; Zhao, X. Tuning Multiscale Microstructures to Enhance Thermoelectric Performance of *n*-Type Bismuth-Telluride-Based Solid Solutions. *Adv. Energy Mater.* **2015**, *5*, 1500411.
5. Yan, X.; Poudel, B.; Ma, Y.; Liu, W.; Joshi, G.; Wang, H.; Lan, Y.; Wang, D.; Chen, G.; Ren, Z. Experimental Studies on Anisotropic Thermoelectric Properties and Structures of *n*-Type  $\text{Bi}_2\text{Te}_{2.7}\text{Se}_{0.3}$ . *Nano Lett.* **2010**, *10*, 3373–3378.
6. Prokofieva, L.; Pshenay-Severin, D.; Konstantinov, P.; Shabaldin, A. Optimum Composition of a  $\text{Bi}_2\text{Te}_{3-x}\text{Se}_x$  Alloy for the *n*-Type Leg of a Thermoelectric Generator. *Semiconductors* **2009**, *43*, 973–976.
7. Liu, W. S.; Zhang, Q.; Lan, Y.; Chen, S.; Yan, X.; Zhang, Q.; Wang, H.; Wang, D.; Chen, G.; Ren, Z. Thermoelectric Property Studies on Cu-Doped *n*-Type  $\text{Cu}_x\text{Bi}_2\text{Te}_{2.7}\text{Se}_{0.3}$  Nanocomposites. *Adv. Energy Mater.* **2011**, *1*, 577–587.
8. Park, K.; Ahn, K.; Cha, J.; Lee, S.; Chae, S. I.; Cho, S.-P.; Ryee, S.; Im, J.; Lee, J.; Park, S.-D.; Han, M. J.; Chung, I.; Hyeon, T. Extraordinary Off-Stoichiometric Bismuth Telluride for Enhanced *n*-Type Thermoelectric Power Factor. *J. Am. Chem. Soc.* **2016**, *138*, 14458–14468.
9. Hu, L.; Zhu, T.; Liu, X.; Zhao, X. Point Defect Engineering of High-Performance Bismuth-Telluride-Based Thermoelectric Materials. *Adv. Funct. Mater.* **2014**, *24*, 5211–5218.
10. Yang, L.; Chen, Z.-G.; Hong, M.; Han, G.; Zou, J. Enhanced Thermoelectric Performance of Nanostructured  $\text{Bi}_2\text{Te}_3$  through Significant Phonon Scattering. *ACS Appl. Mater. Interfaces* **2015**, *7*, 23694–23699.
11. Xu, B.; Feng, T.; Agne, M. T.; Zhou, L.; Ruan, X.; Snyder, G. J.; Wu, Y. Highly Porous Thermoelectric Nanocomposites with Low Thermal Conductivity and High Figure of Merit from Large-Scale Solution-Synthesized  $\text{Bi}_2\text{Te}_{2.5}\text{Se}_{0.5}$  Hollow Nanostructures. *Angew. Chem. Int. Ed.* **2017**, *129*, 3600–3605.

12. Zhao, L.; Zhang, B.-P.; Li, J.-F.; Zhang, H.; Liu, W. Enhanced Thermoelectric and Mechanical Properties in Textured *n*-Type Bi<sub>2</sub>Te<sub>3</sub> Prepared by Spark Plasma Sintering. *Solid State Sci.* **2008**, *10*, 651–658.
13. Li, D.; Li, J.; Li, J.; Wang, Y.; Zhang, J.; Qin, X.; Cao, Y.; Li, Y.; Tang, G. High Thermoelectric Performance of *n*-Type Bi<sub>2</sub>Te<sub>2.7</sub>Se<sub>0.3</sub> via Nanostructure Engineering. *J. Mater. Chem. A*, **2018**, *6*, 9642–9649.